

Naval Command,
Control and Ocean
Surveillance Center

RDT&E Division

San Diego, CA
92152-5001

AD-A267 570

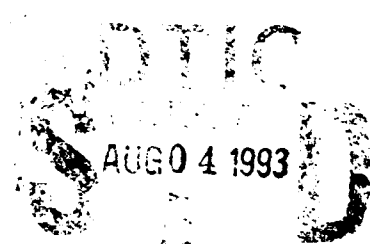


2

Technical Report 1569
January 1993

Measurements of the Radar Cross Section and Inverse Synthetic Aperture Radar (ISAR) Images of a Piper Navajo at 9.5 GHz and 49 GHz

R. Dinger
G. Kinzel
W. Lam
S. Jones



For information
on this product-
contact and

93-17414



424
573
4805



Approved for public release; distribution is unlimited.

92 0 0 1 2

DISCLAIMER NOTICE



THIS DOCUMENT IS BEST QUALITY AVAILABLE. THE COPY FURNISHED TO DTIC CONTAINED A SIGNIFICANT NUMBER OF COLOR PAGES WHICH DO NOT REPRODUCE LEGIBLY ON BLACK AND WHITE MICROFICHE.

Technical Report 1569
January 1993

**Measurements of the Radar Cross Section
and Inverse Synthetic Aperture Radar
(ISAR) Images of a Piper Navajo at 9.5 GHz
and 49 GHz**

R. Dinger
G. Kinzel
W. Lam
S. Jones

**NAVAL COMMAND, CONTROL AND
OCEAN SURVEILLANCE CENTER
RDT&E DIVISION
San Diego, California 92152-5000**

J. D. FONTANA, CAPT, USN
Commanding Officer

R. T. SHEARER
Executive Director

ADMINISTRATIVE INFORMATION

The study covered in this document was performed from December 1990 to December 1992 and was funded by the Space and Naval Warfare Systems Command, Code 44, Washington, DC. The task was performed under program element 0603013N, task no. 75-SX10, accession no. DN309101, and project no. SXB2 by Code 755 of the Naval Command, Control and Ocean Surveillance Center (NCCOSC) RDT&E Division (NRaD), San Diego, California 92152-5001.

Released by
R. J. Dinger, Head
Radar Branch

Under authority of
J. E. Griffin, Head
Electromagnetic
Systems Division

RT

EXECUTIVE SUMMARY

OBJECTIVE

This report investigates the enhanced radar cross section (RCS) and improved inverse synthetic aperture radar (ISAR) image quality that may result at millimeter-wave (mmw) frequencies. To study the potential for mmw radar in these areas, we initiated a program in FY 90 to design and fabricate a 49.0- to 49.5-GHz stepped-frequency radar. The objectives of the measurements with this radar are to

- Determine the radar cross sections of various air and ship targets at 49 GHz and compare them with simultaneous measurements taken of the radar cross sections at 9.5 GHz (X-band).
- Investigate the features of ISAR images at 49 GHz.

RESULTS

After conducting simultaneous measurements of the RCS of an airborne Piper Navajo twin-engine aircraft at 9.0 GHz and 49.0 GHz, the RCS at 49 GHz was always found to be higher than at 9 GHz by an amount that depended on the target-aspect angle. The largest increase was 19 dB and was measured at nose-on incidence; at other angles of incidence, the increase ranged from 3 to 10 dB. The increase averaged over a 360-degree aspect-angle change was 8 dB.

The 49-GHz radar has demonstrated a capability to gather well-calibrated millimeter-wave RCS data of flying targets.

RECOMMENDATIONS

The successful ISAR images obtainable with short aperture time suggest that 49-GHz radar may have a role to play in noncooperative target identification (NCTI).

DTIC QUALITY INSPECTED 3

Accession For	
NTIS GRA&I	<input checked="checked" type="checkbox"/>
DTIC TAB	<input type="checkbox"/>
Unannounced	<input type="checkbox"/>
Justification	
By	
Distribution/	
Availability Codes	
Dist	Availability and/or Special
A-1	

CONTENTS

1.0 INTRODUCTION	1
2.0 49-GHz RADAR	3
2.1 S-BAND RADAR COMPONENTS INCORPORATED INTO THE 49-GHz RADAR	4
2.2 MILLIMETER-WAVE SECTION OF THE RADAR	5
3.0 9.5-GHz RADAR	9
4.0 CALIBRATION	11
4.1 PROCEDURE	11
4.2 ACCOUNTING FOR ATMOSPHERIC ATTENUATION	14
4.3 MINIMUM MEASURABLE RCS	16
5.0 TARGET	19
6.0 TARGET TRACKING	21
7.0 RCS MEASUREMENTS	23
7.1 CIRCULAR-ORBIT RUN	23
7.2 INBOUND RADIAL RUN	31
7.3 DISCUSSION	31
8.0 INVERSE SYNTHETIC APERTURE RADAR (ISAR) IMAGES	37
8.1 ISAR BACKGROUND	37
8.2 ISAR IMAGES	39
9.0 SUMMARY AND CONCLUSIONS	49
10.0 REFERENCES	51

FIGURES

1. Block diagram of the 49-GHz radar. The blocks to the left and below the dashed line are components of an S-band radar designed and fabricated in 1984. The remaining blocks are the components forming the millimeter-wave radar	3
2. Antenna Pedestal.	7
3. Range profile of the 49-GHz return from a calibration sphere suspended beneath a helicopter. The range profile is the Fourier transform of the stepped-frequency returns using a Hamming window	12

4. Thirty-second time history of the RCS (averaged over the 500-MHz radar bandwidth) for the return from the pole-mounted Luneburg lens	13
5. Range profile of the 49-GHz return from a corner reflector mounted on the calibration tower	14
6. Atmospheric attenuation	16
7. Minimum-measurable RCS	17
8. Piper Navajo target	19
9. Track plot for a nearly circular orbit flown by the Piper Navajo target. The numbers beside the track are the burst numbers at that point in the flight	24
10. (a) X-band RCS as a function of time for circular-orbit flight	25
(b) 49-GHz RCS as a function of time for circular-orbit flight. $\alpha_1 = 1.0$ dB/km	26
11. (a) X-band RCS of figure 10(a), averaged over a 1.0-degree window, presented in polar format	27
(b) 49-GHz RCS of figure 10(b), averaged over a 1.0-degree window, presented in polar format	28
12. (a) Histogram of X-band data presented in figure 10(a)	29
(b) Histogram of 49-GHz data presented in figure 10(b)	30
13. (a) X-band RCS as a function of distance during a radial inbound flight	32
(b) 49-GHz RCS as a function of distance during a radial inbound flight. $\alpha_1 = 1.0$ dB/km	33
14. Photograph of cooling fins on the Piper Navajo	35
15. Processing steps for forming an ISAR image	38
16. 49-GHz ISAR image taken during circular-orbit flight	41
17. X-band ISAR image taken during circular-orbit flight	43
18. 49-GHz ISAR image taken during circular-orbit flight	47

TABLES

1. 49-GHz radar parameters	4
2. X-band radar parameters	9
3. Summary of RCS values	31
4. RCS dependence of common scatters in the high-frequency limit	34
5. Parameters used for ISAR images	39

1.0 INTRODUCTION

A radar operating in the millimeter-wave (mmw) band (approximately 35 to 95 GHz) potentially has a number of advantages for surveillance and weapon-control applications. Some advantages accrue from the shorter wavelength: For a given antenna aperture, narrower beam widths and lower side-lobe levels can be obtained, compared to lower frequencies; or, for a given desired set of beam properties, a smaller aperture can be used. Other advantages arise from the atmospheric attenuation at mmw frequencies, including low probability of intercept (LPI) and increased immunity to antiradiation missiles.

In this report, we are particularly interested in the enhanced radar cross section (RCS) and improved inverse synthetic aperture radar (ISAR) image quality that may result at mmw frequencies. To investigate the potential for mmw radar in these areas, we initiated a program in FY 90 to design and fabricate a 49.0- to 49.5-GHz stepped-frequency radar. The objectives of the measurements with this radar are to

- Determine the radar cross sections of various air and ship targets at 49 GHz and compare them with simultaneous measurements taken of the RCS at 9.5 GHz (X-band) and
- Investigate the features of ISAR images at 49 GHz.

The fabrication and test of this radar was completed in January 1992, and measurements were begun in February 1992 on a variety of targets. This report presents the results of the first measurements made with the radar on an aircraft target: a twin-engine propeller-driven Piper Navajo. Coherent stepped-frequency measurements were taken over a 500-MHz bandwidth while the target performed circular orbits and inbound radial flights. Simultaneous comparison measurements were taken with a second radar at 9.5 GHz during these maneuvers.

In Chapter 2, we summarize the design of the 49-GHz radar; and in Chapter 3, we very briefly describe the X-band radar. In Chapter 4, the calibration measurements and procedures are covered, including the manner in which atmospheric attenuation is taken into account. These are presented in some detail because the accuracy of the calibration is particularly important for this program. Chapters 5 and 6 cover the details of the target and target-tracking techniques, respectively. We discuss the RCS measurements and ISAR images in Chapters 7 and 8, respectively, and present conclusions in Chapter 9.

2.0 49-GHz RADAR

The 49-GHz radar is an experimental, data-collection radar built around an existing NRaD data-collection radar that operates at 3 GHz (S-band). The radar is coherent and uses a stepped-frequency waveform covering a 500-MHz bandwidth. Figure 1 is a simplified block diagram of the radar, showing the millimeter-wave RF section and the S-band "backend." A summary of the radar parameters is given in table 1, and descriptions of the radar components are given in the following paragraphs.

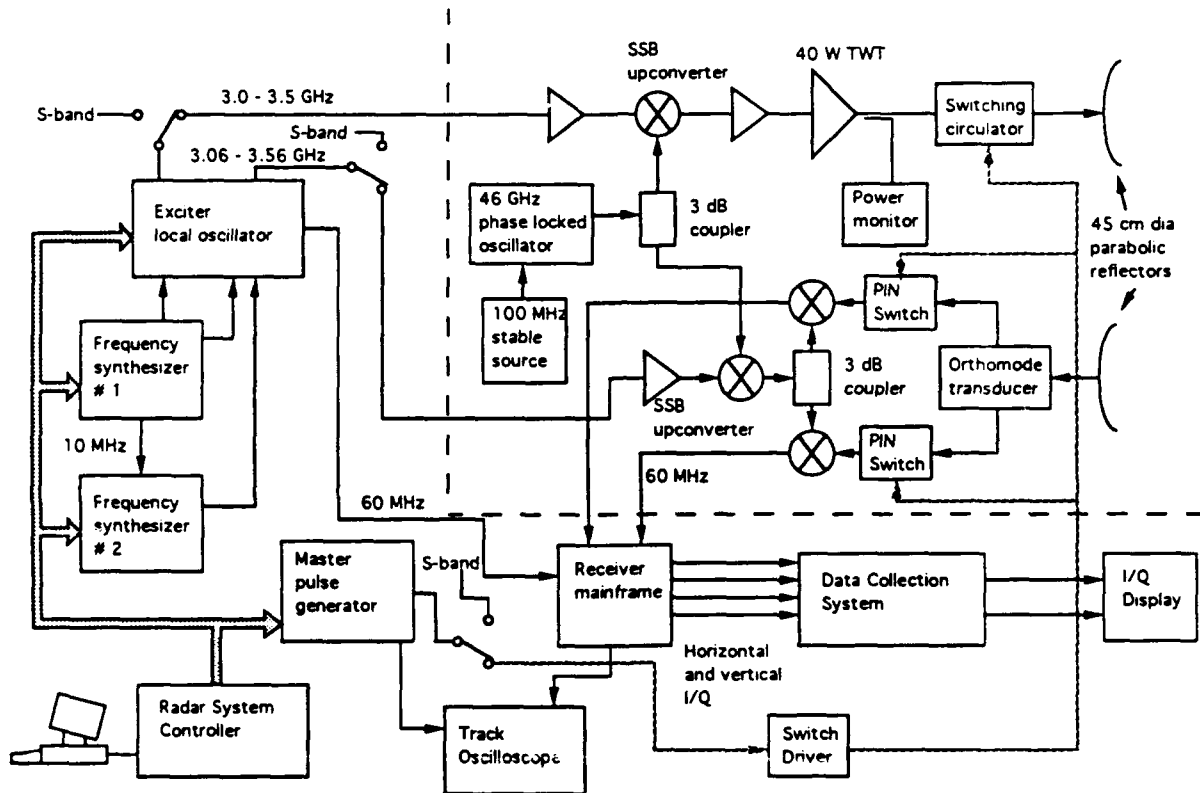


Figure 1. Block diagram of the 49-GHz radar. The blocks to the left and below the dashed line are components of an S-band radar designed and fabricated in 1984. The remaining blocks are the components forming the millimeter-wave radar.

Table 1. 49-GHz radar parameters.

Parameter	Value
Frequency range	49.0 to 49.5 GHz
Bandwidth	0.5 GHz
Waveform	
Type	Stepped frequency
Number of frequencies	32 to 512
Transmitter	
Type	Traveling-wave tube
Peak pulse power	40 W
Pulse width	5 μ sec (typical)
PRF	10 kHz (typical)
Duty factor	0.05
Polarization	Vertical or horizontal (selectable by mechanical change)
Receiver	2 channel, co- and cross-polarization
Antennas	
Type	2 Cassegrain-fed parabolic reflectors
Diameter	45 cm
Beam width (3-dB points)	1.0 deg

2.1 S-BAND RADAR COMPONENTS INCORPORATED INTO THE 49-GHz RADAR

The radar system controller is a digital control system based on a Motorola 68000 microprocessor. The controller provides the command functions for selecting parameters and controlling the bus system that connects the components of the radar. Parameters are selected by a keyboard and CRT readout.

The master pulse generator supplies all the timing pulses controlled by the radar system controller. The master pulse generator also automatically tracks target range.

The basic RF signal is generated by a frequency synthesizer referenced to a stable 10-MHz crystal source. The output of the synthesizer is a cw signal of 1530 to 1780 MHz, which is input to the exciter-local-oscillator (LO) chassis along with the 10-MHz signal; the radar system controller controls frequency selection. Frequency switching time is under 20 microseconds.

The exciter-LO provides additional conditioning of the RF signal. The input frequency is doubled, and the transmit RF drive and LO signals are supplied as outputs. The RF drive is a pulsed RF signal at a frequency of 3.0 to 3.5 GHz. The local oscillator output is a cw signal ranging from 3.060 to 3.560 GHz. In addition, a 60-MHz signal is derived from the 10-MHz source and supplied to the in-phase/quadrature (IQ) detector in the receiver mainframe.

The receiver mainframe consists of two receive channels operating at the 60-MHz intermediate frequency (IF) with inputs from the receiver down converter. The IQ detectors detect the received signal so that both phase and amplitude information is recovered from each pulse. Automatic gain control (AGC) is also implemented in this chassis using digitally controlled attenuators in each channel that are stepped in 1.0-dB increments over a 60-dB range. The output of this unit is four channels of bipolar video (the in-phase and quadrature outputs of the horizontal and vertical channels).

The data-collection system receives the IQ output from the receiver. The IQ data are digitized by the 12-bit analog-to-digital converters and stored on nine-track magnetic tape. In addition to the IQ data, file header and burst header data are stored. The file header contains information on all the fixed parameters of a data run, such as PRF and pulse width. A single file header is appended to a data run. The burst header contains all the dynamic information of each burst, such as target range, antenna pointing angle, and AGC value. A burst consists of the frequency set used in the stepped-frequency waveform. For instance, a typical burst might contain 64 frequencies, with a step size of 7 MHz; the radar would then start at some initial frequency f_0 and increment 7 MHz for each transmit pulse for a total of 64 frequencies to cover nearly 500 MHz. At the end of this sequence, the frequency returns to f_0 and repeats the sequence.

All data processing is performed off line in the Radar Branch's data processing laboratory.

2.2 MILLIMETER-WAVE SECTION OF THE RADAR

The 49-GHz radar uses a 46-GHz phase-locked oscillator and a single-sideband up-converter to translate the 3.0- to 3.5-GHz transmit drive signal from the S-band radar to a 49.0- to 49.5-GHz signal. Similarly, the local-oscillator drive of 3.06 to 3.56 GHz is translated to 49.06 to 49.56 GHz for use as the local-oscillator signal for the mixers.

On the transmit side, the pulsed signal is filtered and amplified to serve as the transmit drive signal. The transmitter source is a 40-W average cw traveling-wave tube (TWT) amplifier. A switching circulator at the output of the TWT is switched into a load during the intrapulse period to prevent coupling the TWT noise into the receiver antenna. A pulse power-monitoring circuit is included at the output of the transmitter.

The transmit antenna is a 45-cm parabolic reflector with a circular waveguide Cassegrain feed. The antenna can transmit either a vertically or horizontally polarized signal, but cannot be switched electrically; a physical change must be made in the waveguide run. All of the data reported here were taken with a vertically polarized transmitted signal.

The receive antenna is identical to the transmit antenna, but the received signal is split into vertical and horizontal components by an orthomode transducer. Switching circulators protect the receiver during the transmit pulse. The received signal is down-converted to 60 MHz in the mixers using the 49.06- to 49.56-GHz local-oscillator signal. The 60-MHz signal is then processed as previously described.

All of the millimeter-wave components are packaged in two units mounted on the antenna pedestal to minimize waveguide losses. The tracking pedestal with antennas is shown in figure 2.

49 GHZ ANTENNAS
TRANSMIT
RECEIVE

X BAND ANTENNA

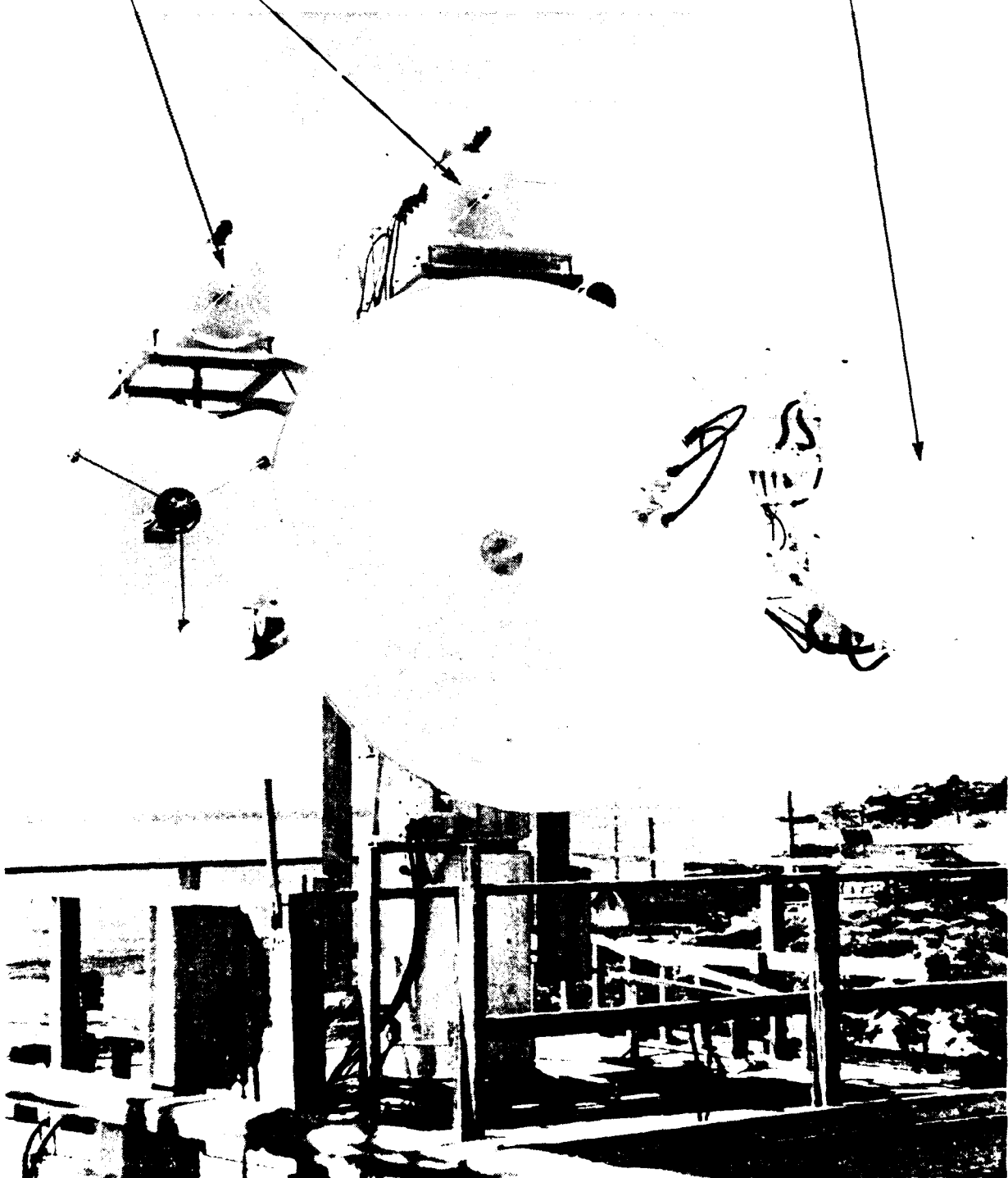


Figure 2. Antenna Pedestal.

3.0 9.5-GHz RADAR

The X-band radar was developed in 1985 for aircraft and ship RCS measurements, and has been used frequently since 1987 (reference 1). The design of the radar has much in common with the S-band radar that serves as the IF and detection stage of the 49-GHz radar (figure 1), and the block diagram is essentially identical. The single X-band antenna (shown in figure 2) has a common boresight with the 49-GHz antennas and a 3-dB beam width of 2.0 degrees. Table 2 summarizes the parameters of the X-band radar.

Table 2. X-band radar parameters.

Parameter	Value
Frequency range	9.0 to 9.5 GHz
Bandwidth	0.5 GHz
Waveform	
Type	Stepped frequency
Number of frequencies	32 to 512
Transmitter	
Type	Traveling-wave tube
Peak pulse power	1 kW
Pulse width	5 μ sec (typical)
PRF	10 kHz (typical)
Duty factor	0.04
Polarization	Vertical or horizontal (switch selectable)
Receiver	Single channel, co- or cross-polarization
Antennas	
Type	Single off-set fed reflector
Size	90 cm
Beam width (3-dB points)	2.5 deg

4.0 CALIBRATION

4.1 PROCEDURE

The X-band and 49.0-GHz radars were calibrated using procedures that have been developed over the past 10 years (reference 1). The primary calibration target is a 1.1-m spun-aluminum sphere suspended below a helicopter on a 400-m length of line. The return from the sphere is measured as the helicopter hovers at ranges from radar-to-sphere of typically 1 to 2 km. The calculated RCS from the sphere is then used to calibrate the radar. Figure 3 shows a typical range profile of a sphere measurement at 49.0 GHz.

Since the helicopter measurement is very expensive, a fixed land-mounted secondary calibration-reference target is needed. To this end, the sphere measurement is used to calibrate the return from a 30-cm-diameter Luneburg lens mounted on a 12-m tower. The tower is located on a ridge 0.5 km from the radar in a configuration that minimizes the reflections from the tower. This lens has been in use for 4 years as a secondary calibration target for the X- and Ku-band radars and has shown good long-term stability. Figure 4 is a plot of a 30-second time history of the average RCS of the Luneburg lens from 49.0 to 49.5 GHz. The X-band calibration gives similar results.

To further verify the calibration accuracy at 49.0 GHz, a trihedral corner reflector was fabricated that was sized to have an RCS of 30.0 dBsm at 49.0 GHz, as given by the standard RCS expression (reference 2). Tight tolerances were maintained in all size and angle measurements, and the interior surfaces were highly polished. The corner reflector was mounted on the calibration tower in place of the Luneburg lens, and the RCS was measured. In figure 5 we show the resulting range profile of the corner reflector, with the RCS value set by the sphere/Luneburg lens sequence of measurements just described. The corner reflector is measured as 29.8 dBsm, a value that confirms the accuracy of the calibration technique.

Our standard procedure during a sequence of target RCS measurements is to (1) carry out a calibration sequence prior to the measurements and then (2) repeat the sequence immediately following the last target measurement. In all of the measurements reported here, differences in the pretest and post-test calibrations were less than 0.5 dB.

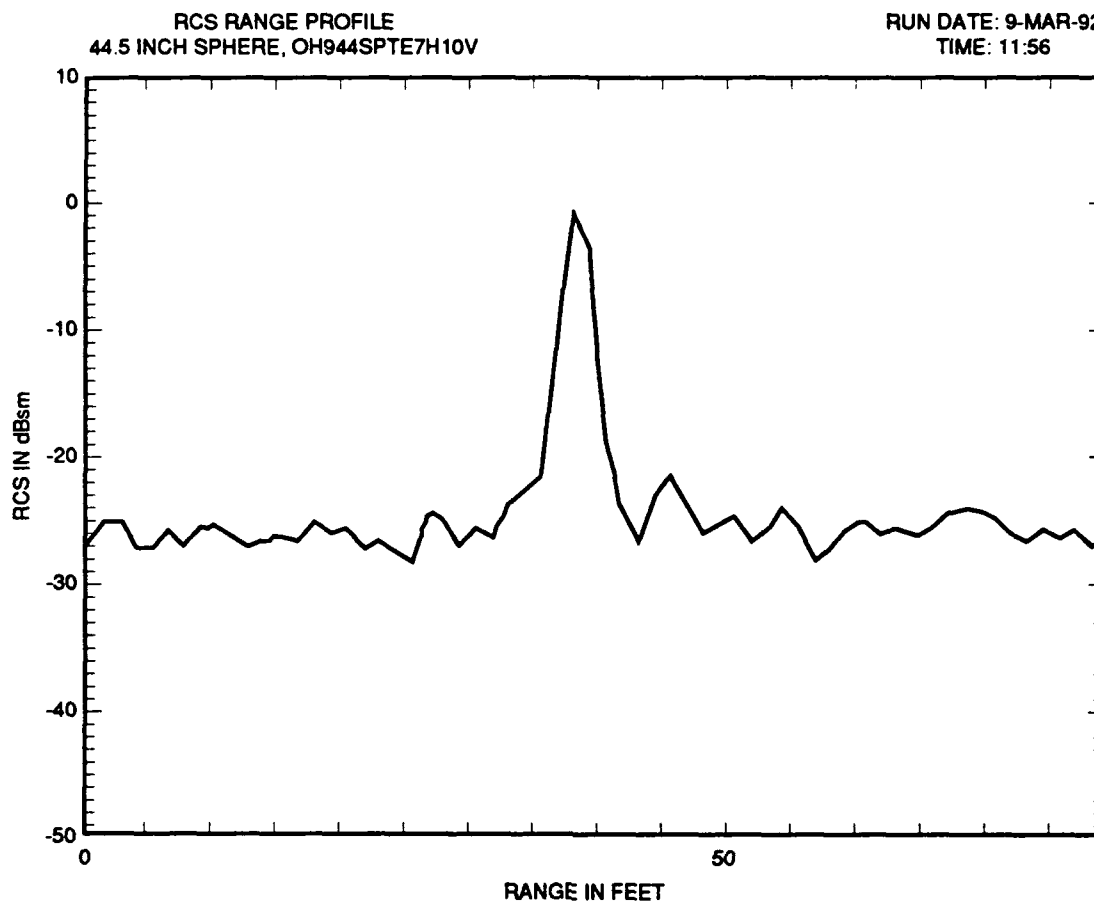


Figure 3. Range profile of the 49-GHz return from a calibration sphere suspended beneath a helicopter. The range profile is the Fourier transform of the stepped-frequency returns using a Hamming window.

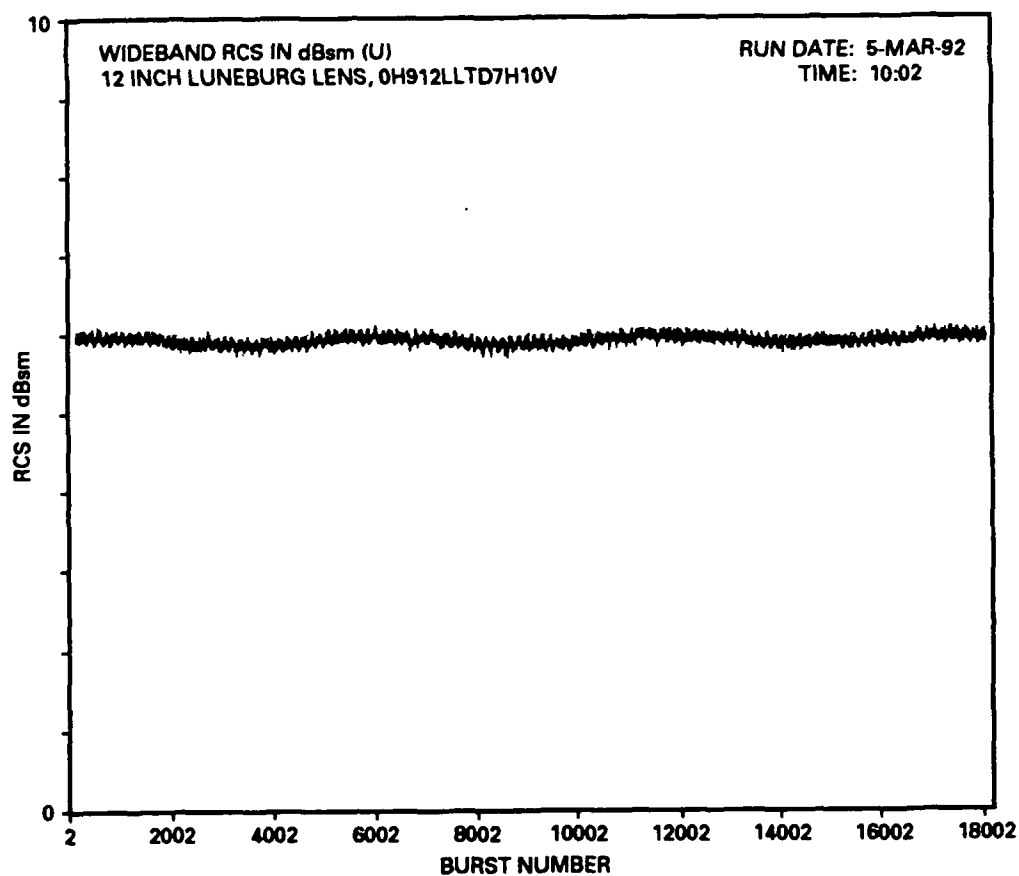


Figure 4. Thirty-second time history of the RCS (averaged over the 500-MHz radar bandwidth) for the return from the pole-mounted Luneburg lens.

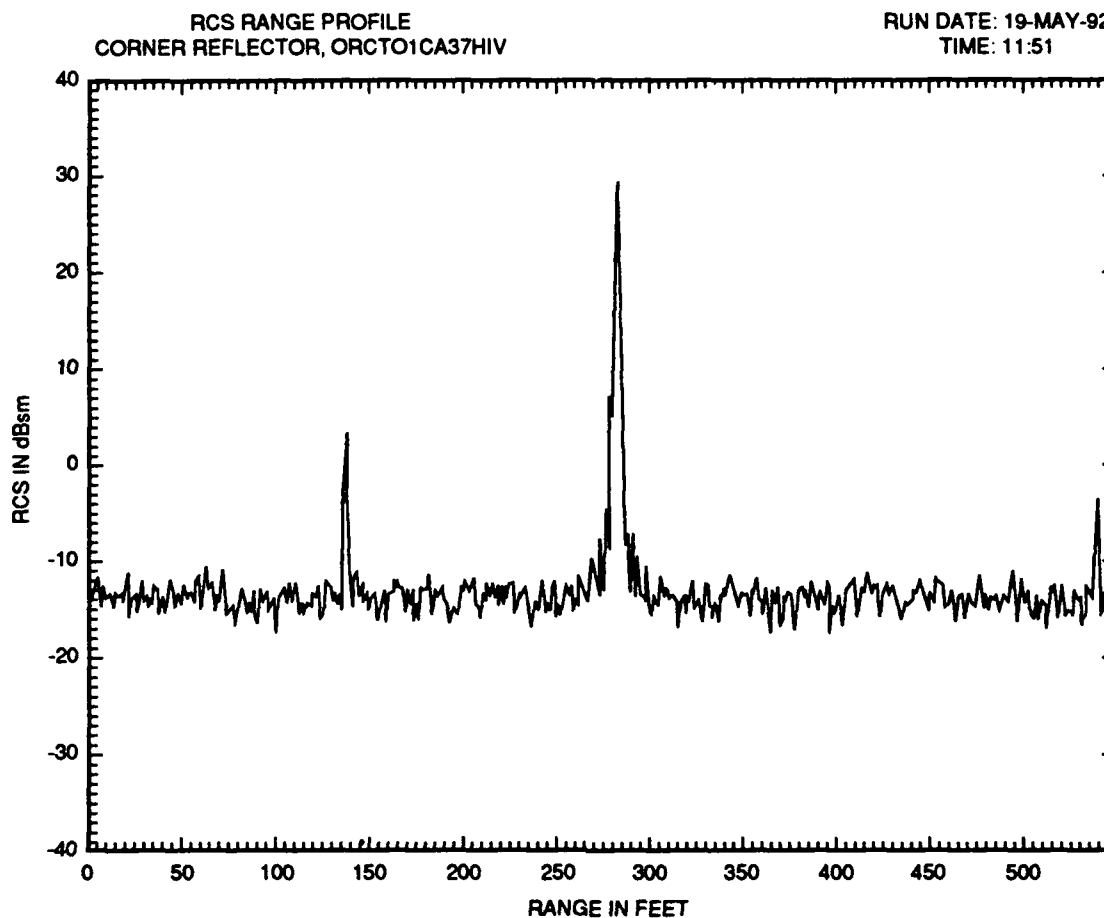


Figure 5. Range profile of the 49-GHz return from a corner reflector mounted on the calibration tower.

4.2 ACCOUNTING FOR ATMOSPHERIC ATTENUATION

As detailed in reference 1, in the absence of atmospheric attenuation, the RCS of a target under test is calculated from

$$\sigma_t = \sigma_c \left(\frac{R_t}{R_c} \right)^4 \left(\frac{P_t}{P_c} \right) \quad (1)$$

where

- σ_t = target-under-test RCS
- σ_c = calibration target RCS
- R_t = range to target
- R_c = range to calibration target
- P_t = measured signal power from target-under-test
- P_c = measured signal power from calibration target

This equation is the basic equation used for the X-band RCS measurements. However, the atmospheric attenuation must be taken into account at 49.0 GHz; in this case, equation (1) is replaced by

$$\sigma_t = \sigma_c \left(\frac{R_t}{R_c} \right)^4 \left(\frac{P_t}{P_c} \right) e^{2(\alpha_t R_t - \alpha_c R_c)} \quad (2)$$

where α_t = one-way atmospheric-attenuation constant during the target measurement (nepers/km)

α_c = one-way atmospheric-attenuation constant during the calibration target measurement (nepers/km)

Hence, the atmospheric-attenuation constant must be measured or estimated to derive the target RCS.

We derive the attenuation coefficient from the model developed by reference 3, using the temperature and humidity measured at the radar site as inputs. The temperature and humidity are assumed to be constant along the propagation path. Since the targets are measured at angles of 6 degrees or less above the horizon, the assumption of a uniform propagation path seems reasonable. Figure 6 is a plot of α_t as derived from the model, indicating the conditions for the measurements reported here. The calculated attenuation constant is $\alpha_t = 0.54$ dB/km.

The fractional error in RCS for an error $\delta\alpha_t$ in attenuation constant can be derived from equation (2):

$$\frac{\delta\sigma_t}{\sigma_t} = 2 R_t \delta\alpha_t \quad (3)$$

Hence, to maintain the error in RCS to less than 0.5 dB, the attenuation constant must be calculated with an error no greater than 0.07 dB/km at a target range of 3.7 km (2 nmi), an error of 12 percent. The model developed in reference 3 is capable of this accuracy, and also supporting the accuracy of the model are the results of several measurements reported below that would be sensitive to errors in the attenuation constant value.

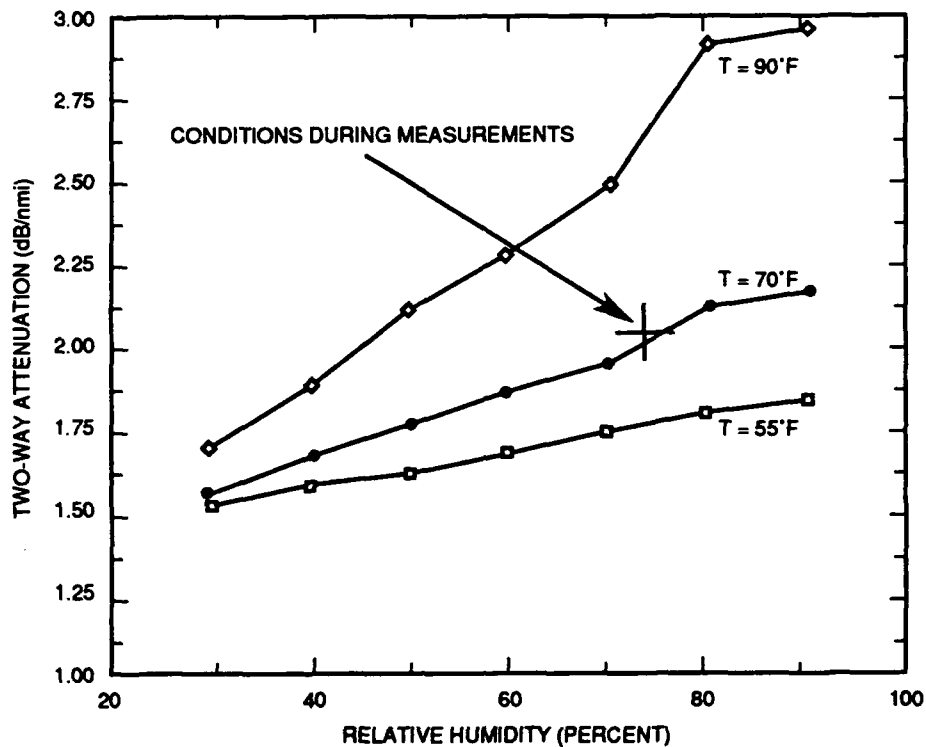


Figure 6. Atmospheric attenuation.

4.3 MINIMUM MEASURABLE RCS

A measurement of the minimum measurable 49-GHz RCS was made by pointing the radar at an elevation angle of 45 degrees in a direction with no target to measure "sky noise." The range gate then was set to move out (in automatic mode) at a constant rate while the receiver output was recorded by the standard data recording system. This tape was then processed in the standard manner (i.e., using equation (2)) to yield the apparent RCS from the radar at a signal-to-noise ratio (SNR) of 0 dB.

The results are shown in figure 7. A curve is plotted for $\text{SNR} \approx 13$ dB, a value representing the minimum acceptable SNR for which a reliable RCS value can be derived. This plot indicates that an RCS of -9 dBsm or higher can be measured at a range of 2 nmi.

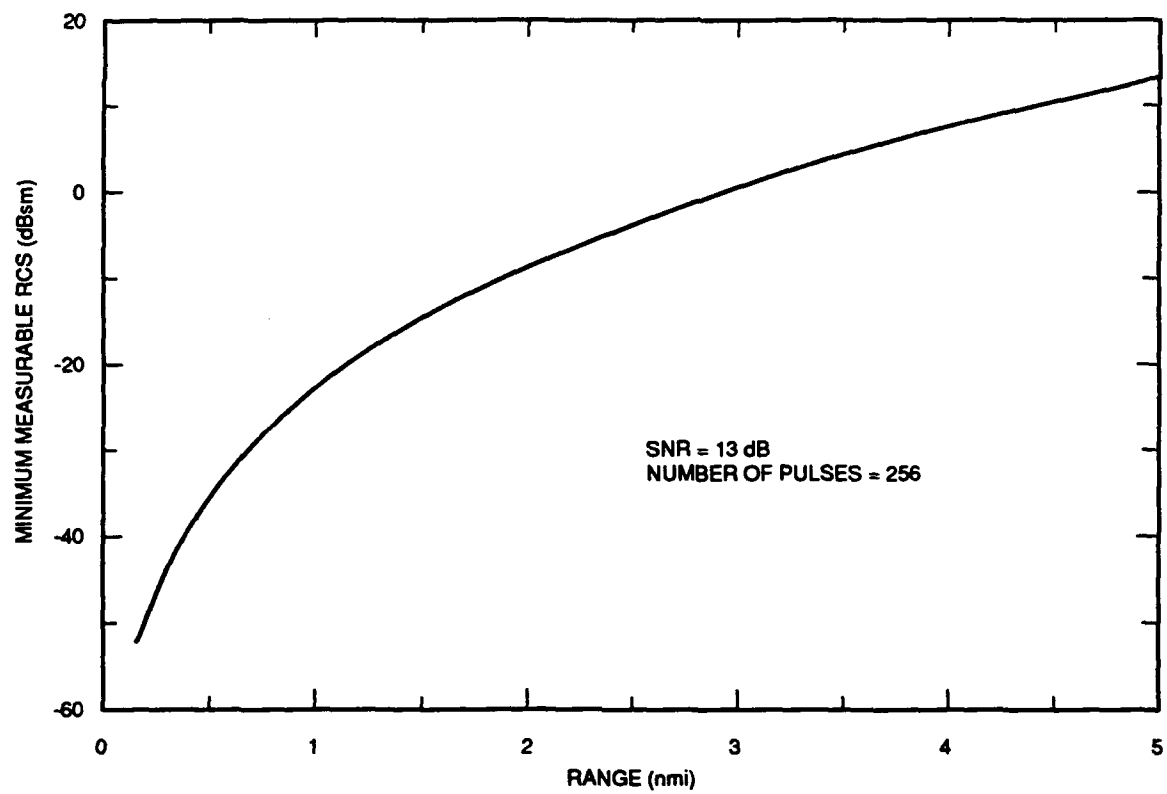


Figure 7. Minimum-measurable RCS.

5.0 TARGET

The services of a Piper Navajo twin-engine aircraft (figure 8) were leased from Gibbs Flying Service, San Diego, CA, for a total of about 2 hours of flight time. The target flew two types of maneuvers: circular orbits at a bank angle of 20 degrees, and straight inward- and outward-bound radials from the radar. The center of the circular orbits was usually about 3.3 km from the radar, and the radius of the orbits was 1.8 km. Elevation for all flights was a nominal 300 m above sea level. All flights were guided by a controller observing a realtime track display at the radar fieldhouse who then radioed instructions to the pilot. During all but the straight-line flights, the pilot called out his compass heading at intervals of 30 degrees.



Figure 8. Piper Navajo target.

6.0 TARGET TRACKING

We tracked the target manually by observing it with a TV camera mounted on the antenna pedestal and using a joy-stick controller to point the pedestal. We have used manual tracking for the X-band radar for many previous series of measurements and can usually keep the target well within the beam during all maneuvers. However, because the beam width of the 49-GHz radar is one-half of the X-band beam width, we could not always keep the target centered in the 49-GHz beam. At a target range of 3.7 km, for example, the 3-dB beam footprint is approximately 60 m, compared with 120 m for the X-band radar.

Evidence of occasional RCS "fades," due to target wander out of the center of the 49-GHz beam, can be seen in some of the data runs. However, the fades were not a serious problem and can usually be identified as such in the data.

7.0 RCS MEASUREMENTS

Here we present the results of two runs. The first is a complete circular orbit at a bank angle of 20 degrees, and the second is an inbound flight along a straight radial at a bank angle of 0 degrees.

7.1 CIRCULAR-ORBIT RUN

A sketch of the flight path for this run is shown in figure 9. The burst numbers are indicated at selected points along the path; these points can be compared with the burst numbers along the abscissa of the RCS plots. The circle does not close on itself because of aircraft drift caused by a wind blowing from the west.

Figures 10(a) and 10(b) present the derived RCS for this run as a function of time. Attached to the time axis (shown as burst number, which corresponds to the burst numbers indicated on the track plot in figure 9) is the target-aspect angle (as defined in figure 8), as derived from the target-heading information announced by the pilot. In figures 11(a) and 11(b), a polar plot is given of the RCS calculated by averaging the values in figures 10(a) and 10(b) over 1.0-degree sectors.

The general shapes of the plots at the two frequencies are similar, but some variations occur in the 49-GHz RCS that probably are manifestations of the tracking limitations discussed in Chapter 6. In particular, the sharp 15-dB decrease near burst 20,000 (aspect angle = 0 degrees) is almost certainly a tracking-induced fade in which the target could not be kept centered in the 49-GHz beam. Some of the variation in RCS between burst 14,000 and 18,000 might also arise from tracking errors. Such tracking variations will tend to underestimate the average RCS at 49 GHz.

The RCS at 49 GHz is higher than the RCS at X-band. Figures 12(a) and 12(b) are RCS histograms, showing that the average 49-GHz RCS over the circular orbit is 7.8 dB higher than the X-band RCS. Specific aspect angles can be compared in figures 10 and 11. Table 3 summarizes the values at key target aspect angles.

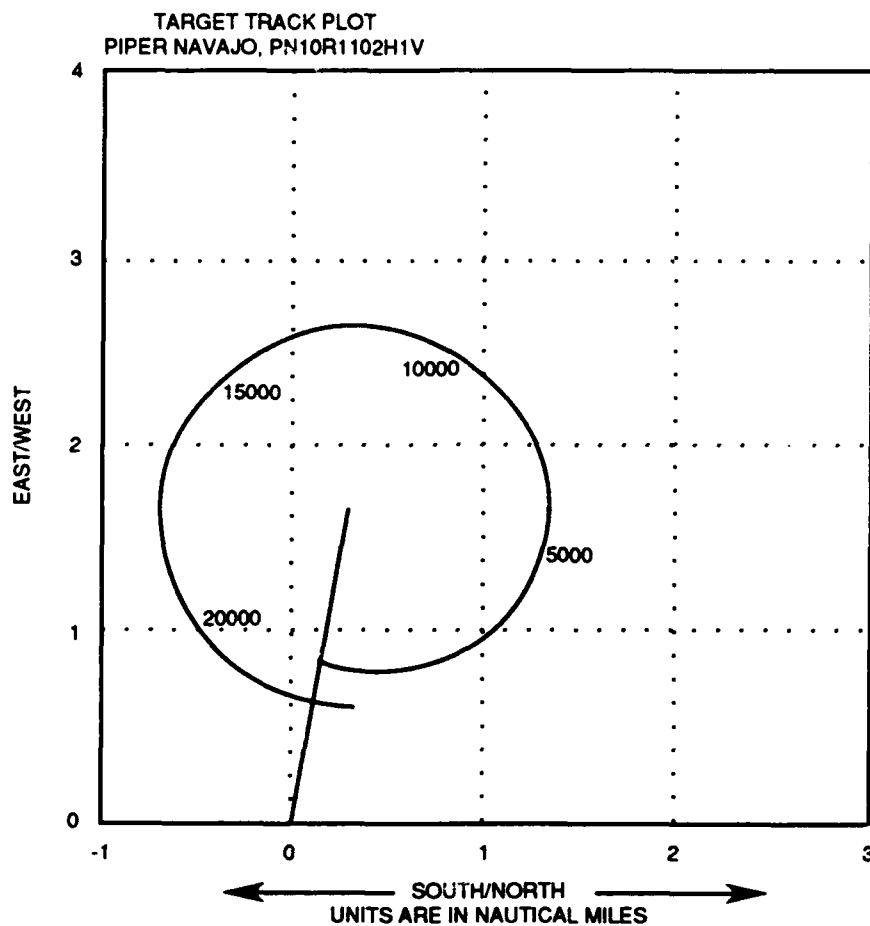


Figure 9. Track plot for a nearly circular orbit flown by the Piper Navajo target. The numbers beside the track are the burst numbers at that point in the flight.

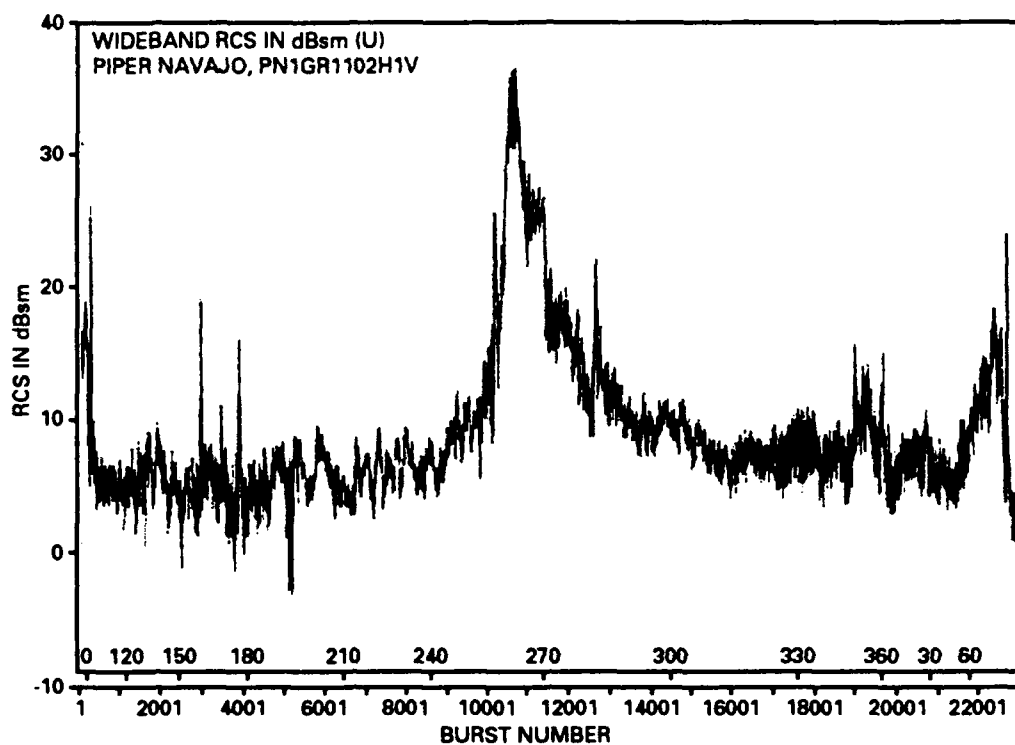


Figure 10(a). X-band RCS as a function of time for circular-orbit flight.

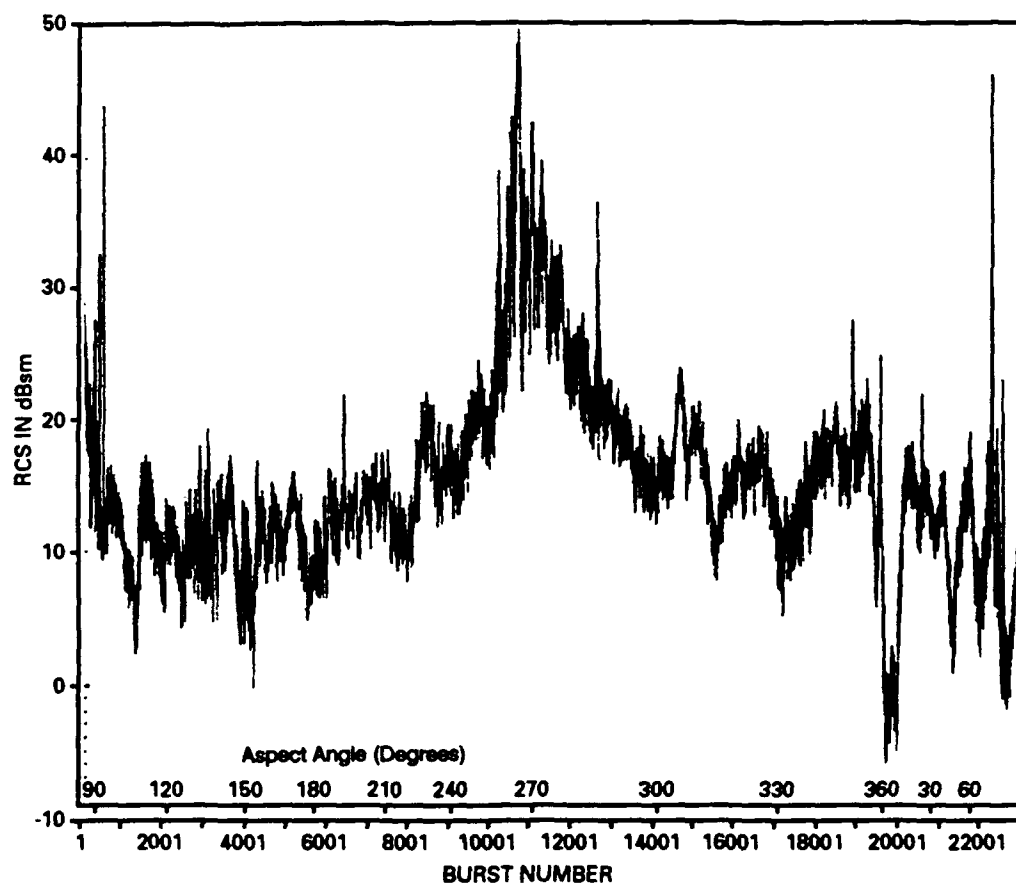


Figure 10(b). 49-GHz RCS as a function of time for circular-orbit flight. $\alpha_t = 1.0$ dB/km.

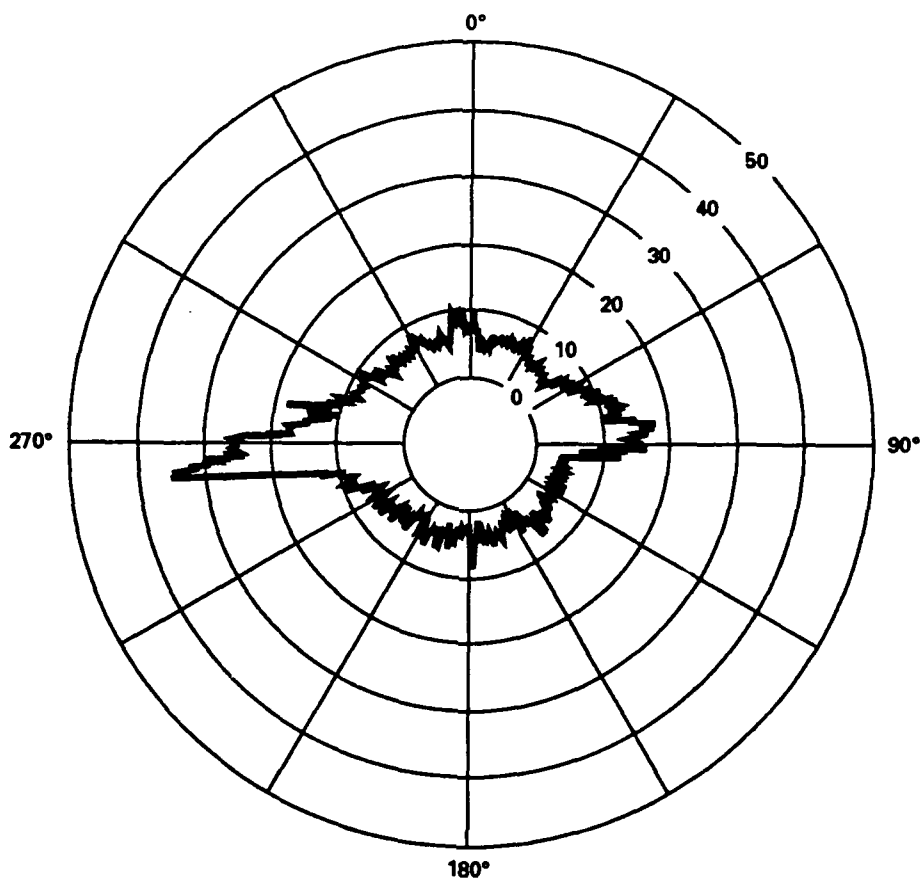


Figure 11(a). X-band RCS of figure 10(a), averaged over a 1.0-degree window, presented in polar format.

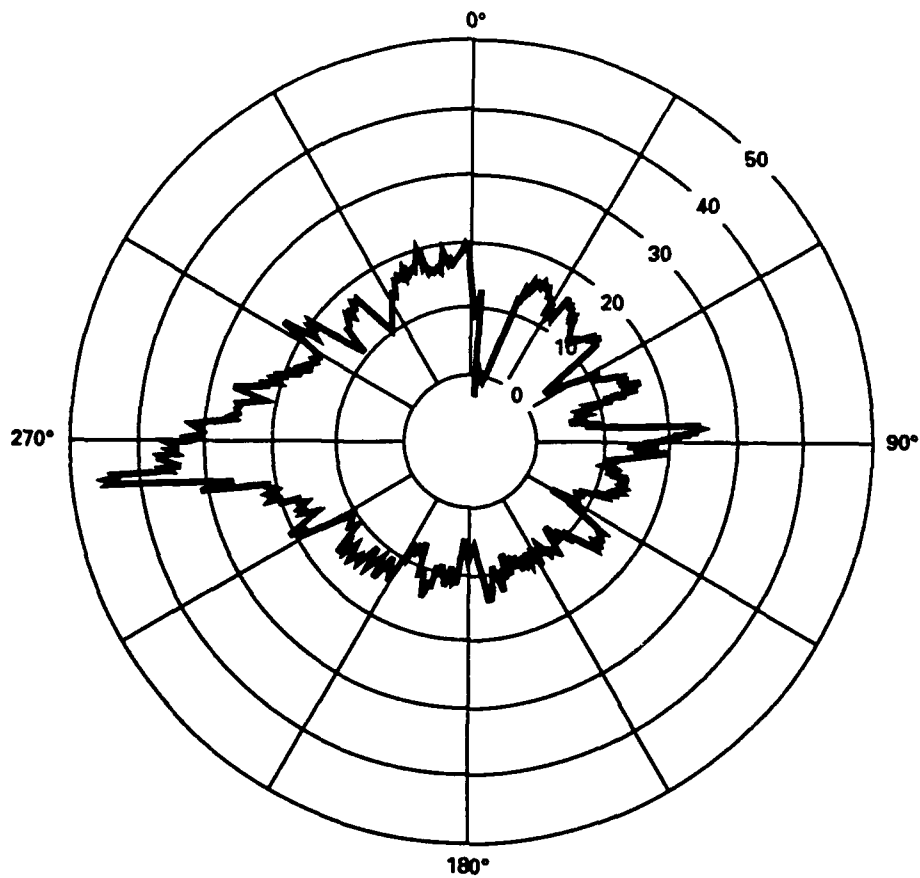


Figure 11(b). 49-GHz RCS of figure 10(b), averaged over a 1.0-degree window, presented in polar format.

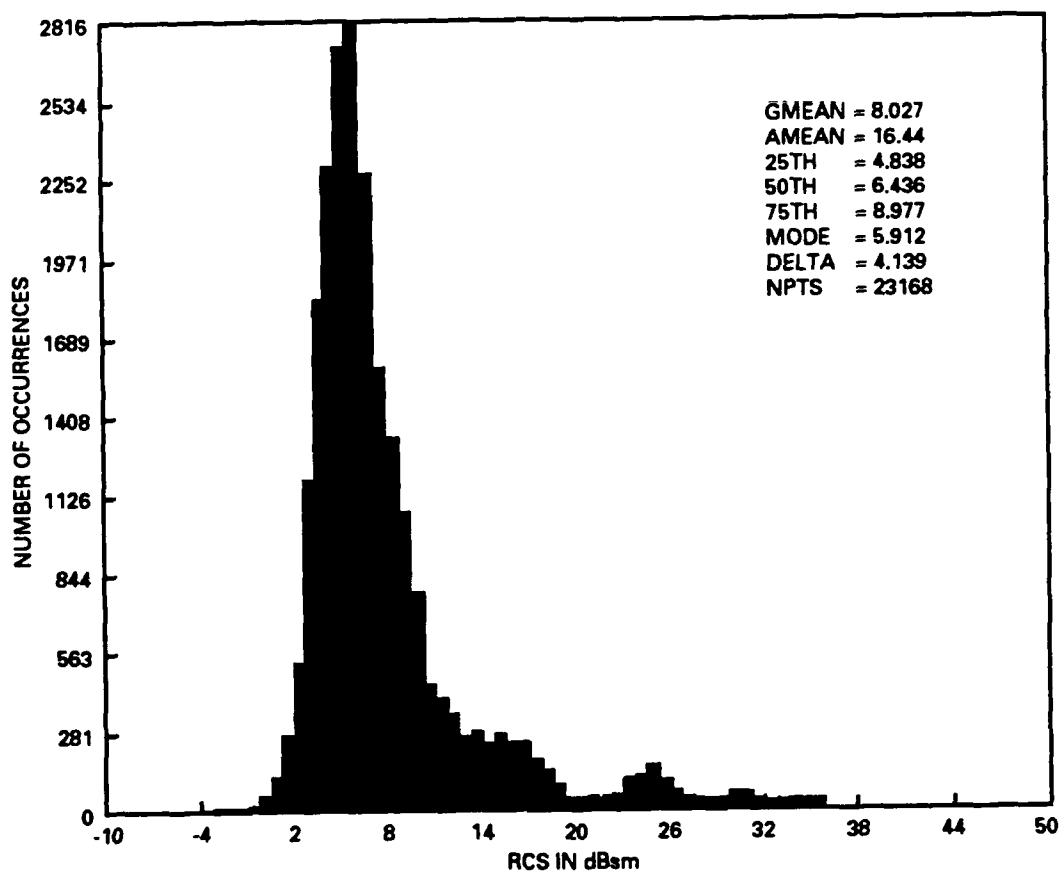


Figure 12(a). Histogram of X-band data presented in figure 10(a).

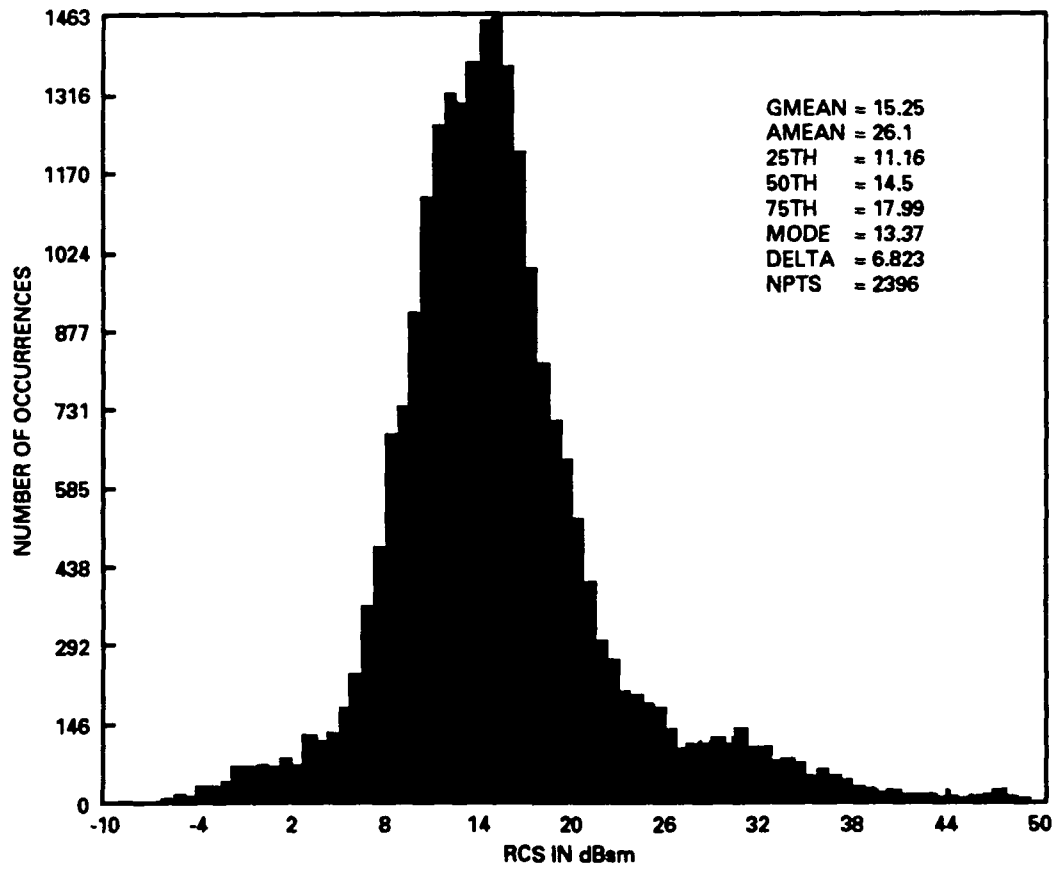


Figure 12(b). Histogram of 49-GHz data presented in figure 10(b).

Table 3. Summary of RCS values.

Aspect and Condition	49-GHz RCS (dBsm)	X-band RCS (dBsm)	RCS Difference (49 GHz - X) (dBsm)	Figure Number
Broadside top	50	35	15	10
Broadside bottom	19	17	2	10
Tail-on	17	14	3	10
Head-on	22	13	9	10
Head-on (radial leg)	26	7	19	13
Mean value (from histograms)	15.2	8.0	7.2	12

7.2 INBOUND RADIAL RUN

The variation in RCS during an inbound flight is shown in figures 13(a) and 13(b). Although the average value of the 49-GHz RCS fluctuates 10 dB, the mean value of the RCS is essentially constant over the 4.6-km (2.5 nmi) range. This constancy indicates that the atmospheric attenuation has been properly accounted for, since an incorrect value would produce a 49-GHz RCS whose mean value changes linearly with range (when expressed in dBsm).

The mean value of the 49-GHz RCS is 19.0 dB higher than the X-band RCS. At first glance, the 27-dBsm average value from figure 13(b) may not appear to agree well with the values near 0-degree aspect angle (head-on) in figure 10(b) measured during the circular-orbit flight. The value at head-on in figure 10(b) is obscured by a tracking dropout, but the value immediately before the dropout is approximately 22 dBsm. In fact, this value is encompassed within the fluctuations observed in figure 13(b). In addition, the target is banked at a 20-degree angle during the circular-orbit flight, compared with a 0-degree bank angle during the inbound radial flight, so that the RCS values could be expected to differ somewhat on this basis.

7.3 DISCUSSION

A complex target at wavelengths short compared to target size can be viewed as a collection of corner reflectors, edges, flat plates, cones, etc. These "scattering centers" produce an RCS that is the coherent summation of the RCS of the individual scattering centers. Neglecting interactions between the scattering centers, the RCS of a complex target can be written as

$$\sigma = \left| \sum_n \sqrt{\sigma_n} e^{j\phi_n} \right|^2 \quad (4)$$

where σ_n is the RCS of the n th scattering center and ϕ_n is the relative phase angle. The phase angle accounts for the difference in range of the scattering centers from the radars, as well as any phase shift produced by the scattering center itself.

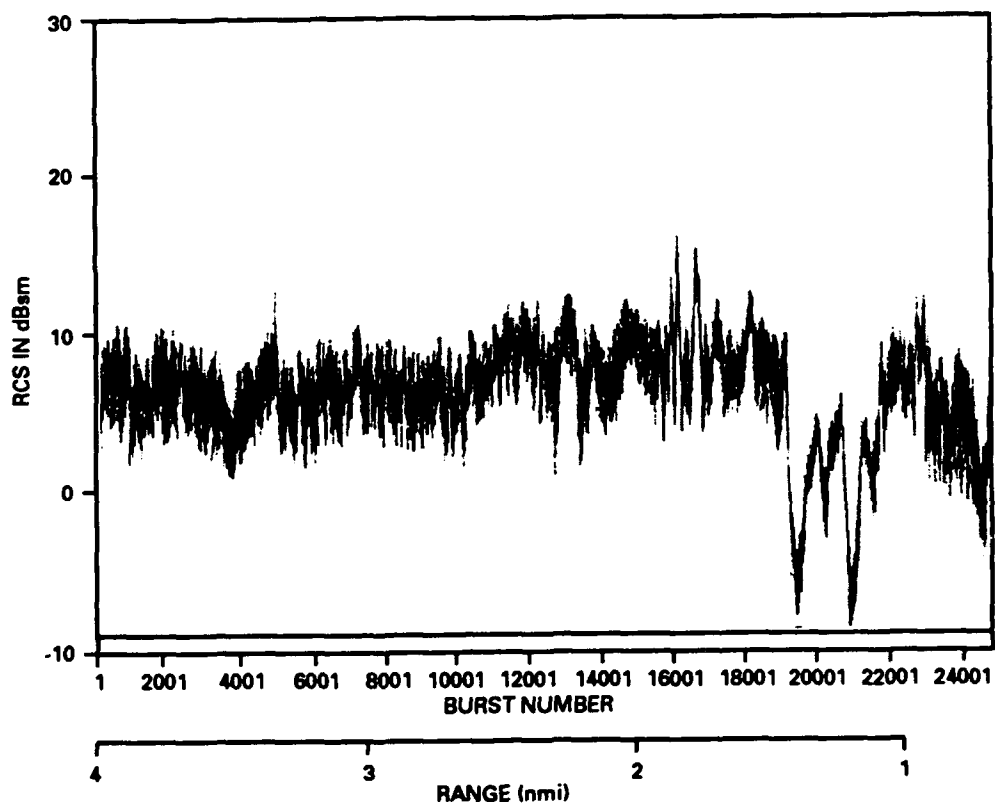


Figure 13(a). X-band RCS as a function of distance during a radial inbound flight.

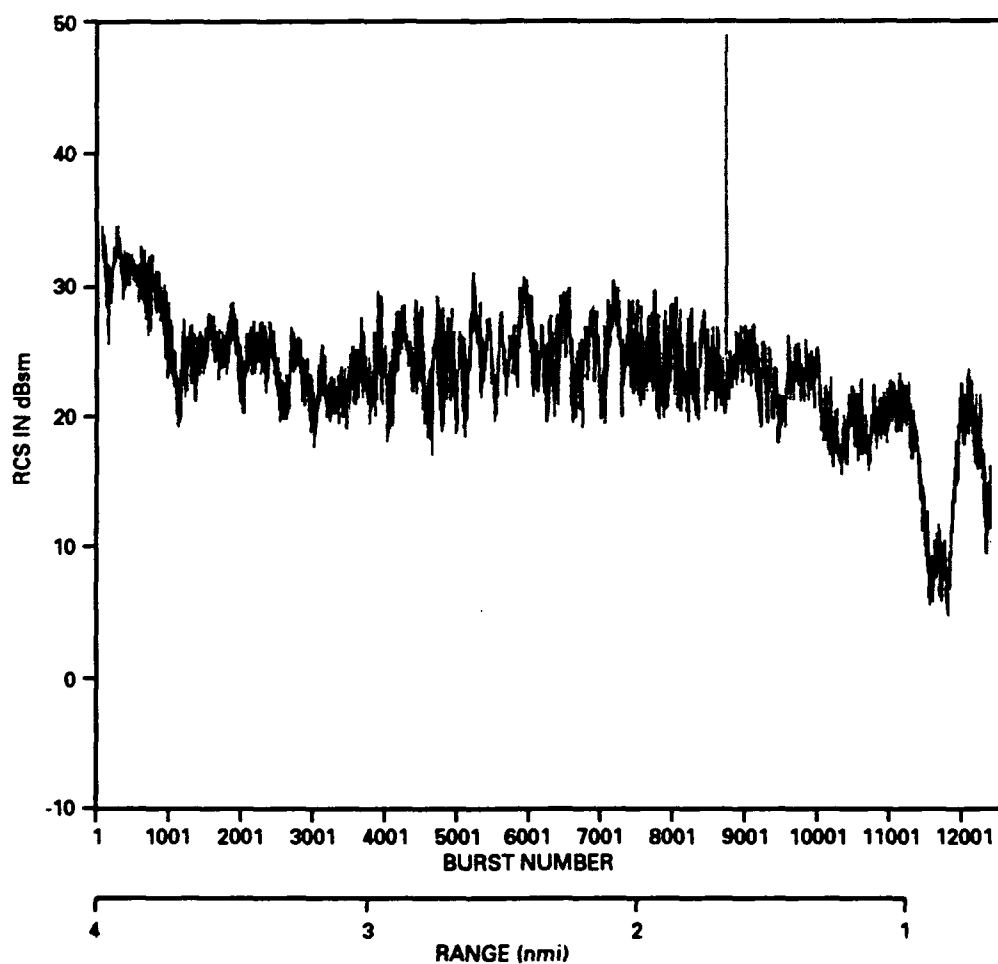


Figure 13(b). 49-GHz RCS as a function of distance during a radial inbound flight. $\alpha_1 = 1.0$ dB/km.

Hence, the frequency dependence of the RCS of individual scattering centers determines the target RCS. Table 4 is a list of the common scattering center types and their frequency dependence. Also given is the relative scattering strength in dB for the $49.0/9.0 = 5.44$ frequency ratio applicable in the present work. This table shows that the target RCS will have a dependence on frequency that is very sensitive to the visible scattering centers—and hence aspect angle—since the individual scattering centers can have a higher or lower RCS as frequency is increased. However, the main scattering centers—both in number and in RCS value—on aircraft targets are flat plates, corner reflectors, cylinders, and similar surfaces that produce an increased RCS at 49 GHz compared to 9 GHz. Thus, the approximate 6- to 9-dB increase measured for the 49-GHz RCS seems reasonable. A detailed calculation of the Piper Navajo RCS using available RCS codes is beyond the scope of this report.

Table 4. RCS dependence of common scatters in the high-frequency limit.

Scattering-Center Type	Frequency Dependence	Amplitude difference between 49.0 and 9.0 GHz (dB)
Corner reflector	f^2	14.7
Flat plate	f^2	14.7
Cylinder (or any singly curved surface)	f^1	7.4
Sphere (or any doubly curved surface)	f^0	0
Curved edge	f^{-1}	-7.4
Cone tip	f^{-2}	-14.7

We are unable to account convincingly for the very large increase of 19 dB at head-on incidence. We have examined the Piper Navajo in detail and have not found any obvious sources of scattering that would clearly enhance a 49-GHz return by this magnitude. A possibility, perhaps, is the series of cooling fins that encase the horizontally opposed cylinders (figure 14). These fins are clearly visible by a radar only at head-on incidence and form a type of grating. Each fin is 1.6 mm wide (0.26 wavelength at 49 GHz), and the spacing between adjacent fins is 2.38 mm (0.39 wavelength), so that the repeat dimension of the grating is 3.98 mm (0.65 wavelength). The total exposed area of this fin structure on two sides of two engines is approximately 650 cm². Grating effects on RCS are usually observed at incidence angles away from the normal to the grating (reference 4), but there may be a resonant effect in the present case that enhances the backscatter. Calculation of the RCS from such a structure is beyond the scope of this report.

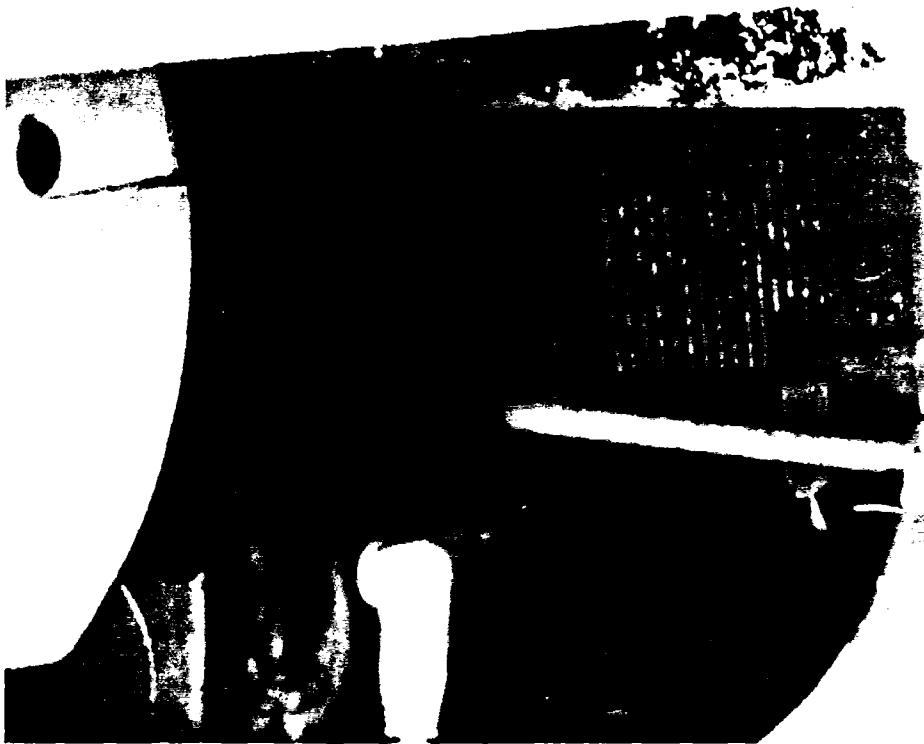


Figure 14. Photograph of cooling fins on the Piper Navajo.

8.0 INVERSE SYNTHETIC APERTURE RADAR (ISAR) IMAGES

8.1 ISAR BACKGROUND

An ISAR image is formed by using bandwidth to resolve scattering centers in the down-range dimension and the differential Doppler shift produced by target motion to resolve scattering centers in the cross-range dimension (reference 5). The image is generated in a two-dimensional range-Doppler space; the pixel sizes are given by

$$\Delta R = \frac{c}{2B} \quad (\text{downrange}) \quad (5)$$

and

$$\Delta f_d = \frac{f_p}{N_b N_f} \quad (\text{Doppler}) \quad (6)$$

where B = bandwidth, N_b = number of pulses in a burst, N_f = number of bursts in a frame, and f_p = pulse repetition frequency. The length of time needed to accumulate the data for a single image is denoted the aperture time and is given by

$$T_f = \frac{N_f N_b}{f_p} \quad (7)$$

If the kinematics of the target are known sufficiently, the Doppler cross-range axis can be converted to meters by the relationship

$$x = \frac{\lambda f_d}{2\Omega} \quad (8)$$

where x is the cross-range dimension and Ω is the angular rate-of-change. The corresponding cross-range pixel size is

$$\Delta x = \frac{\lambda \Delta f_d}{2\Omega} \quad (9)$$

The images are presented in range-Doppler coordinates.

The steps to form an ISAR image are shown in figure 15; a thorough discussion of these steps can be found in reference 5. The motion-compensation technique used for these images has been described in reference 6.

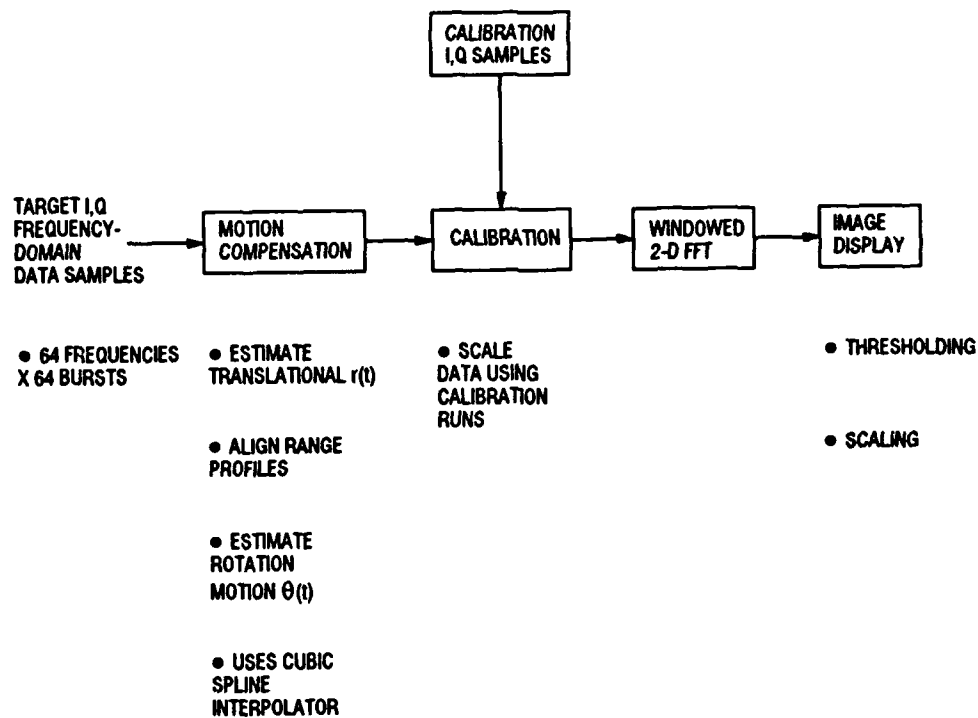


Figure 15. Processing steps for forming an ISAR image.

8.2 ISAR IMAGES

Table 5 lists the waveform and processing parameters for the ISAR image runs. Figure 16 is an ISAR image taken during the circular-orbit run from which the RCS results of figure 10 were derived. For comparison, an X-band image taken at nearly the same time is shown in figure 17. Several points should be emphasized in the comparison of these images:

- The radar is located on the right side for the 49-GHz image and is located on the left side for the X-band image. That is, to compare images, one should mentally flip one of them in the horizontal direction (this circumstance occurred because of a difference in sign in the quadrature detectors between the X-band and 49-GHz radars).

Table 5. Parameters used for ISAR images.

Parameter	Symbol	Equation Number	Value
Bandwidth	B		0.5 GHz
Pulse-repetition frequency	f_p		10 kHz
Number of pulses in a burst	N_b		64
Number of bursts in a frame	N_f		64
Frame time	T_f	6	0.41 sec
Downrange pixel size	ΔR	4	30 cm
Doppler pixel size	Δf_d	5	2.44 Hz
Target turn rate*	Ω		43 mrad/sec
Cross-range pixel size	Δx	9	
X-band			93 cm
49 GHz			17 cm
Target-turn rate for $\Delta x = \Delta R$	Ω_o	10	
X-band			134 mrad/sec
49 GHz			25 mrad/sec

*Computed turn rate during circular orbit.

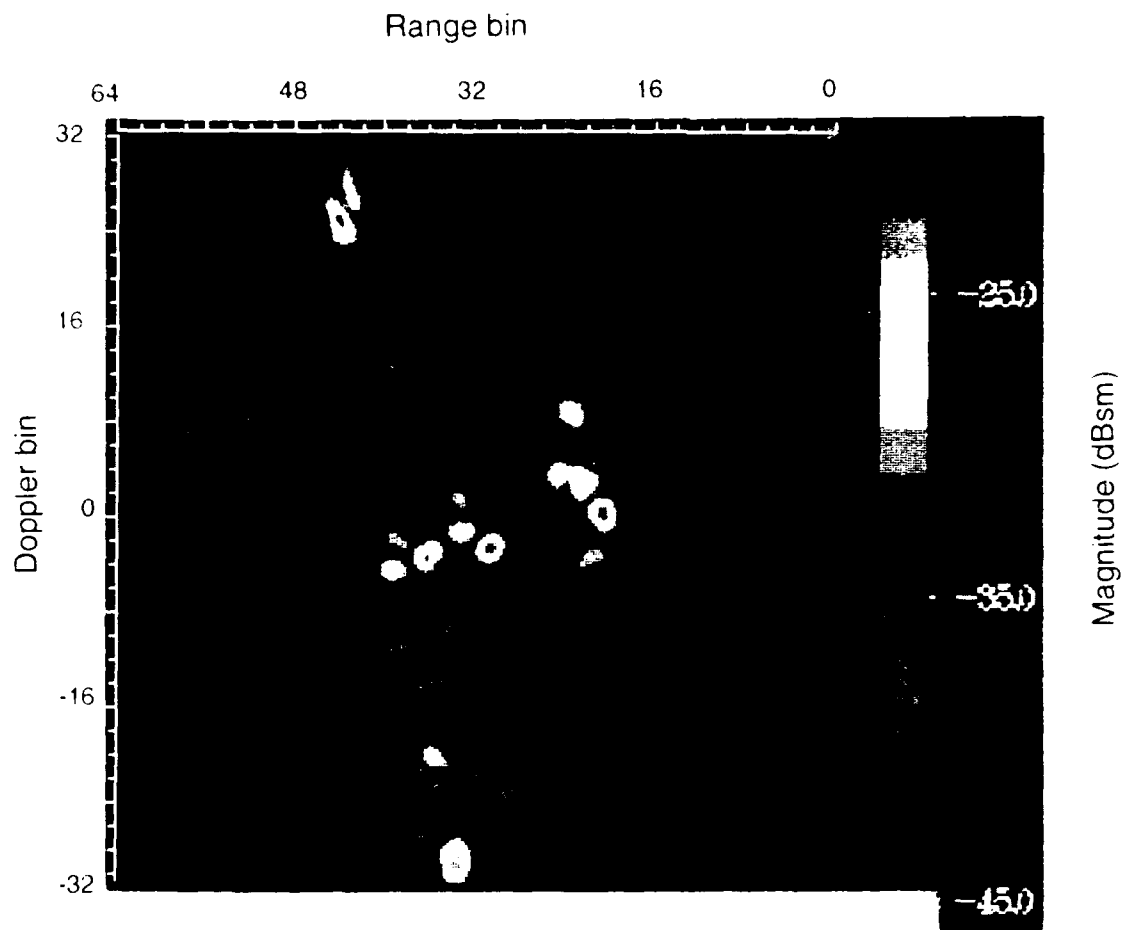


Figure 16 49-GHz ISAR image taken during circular-orbit flight.

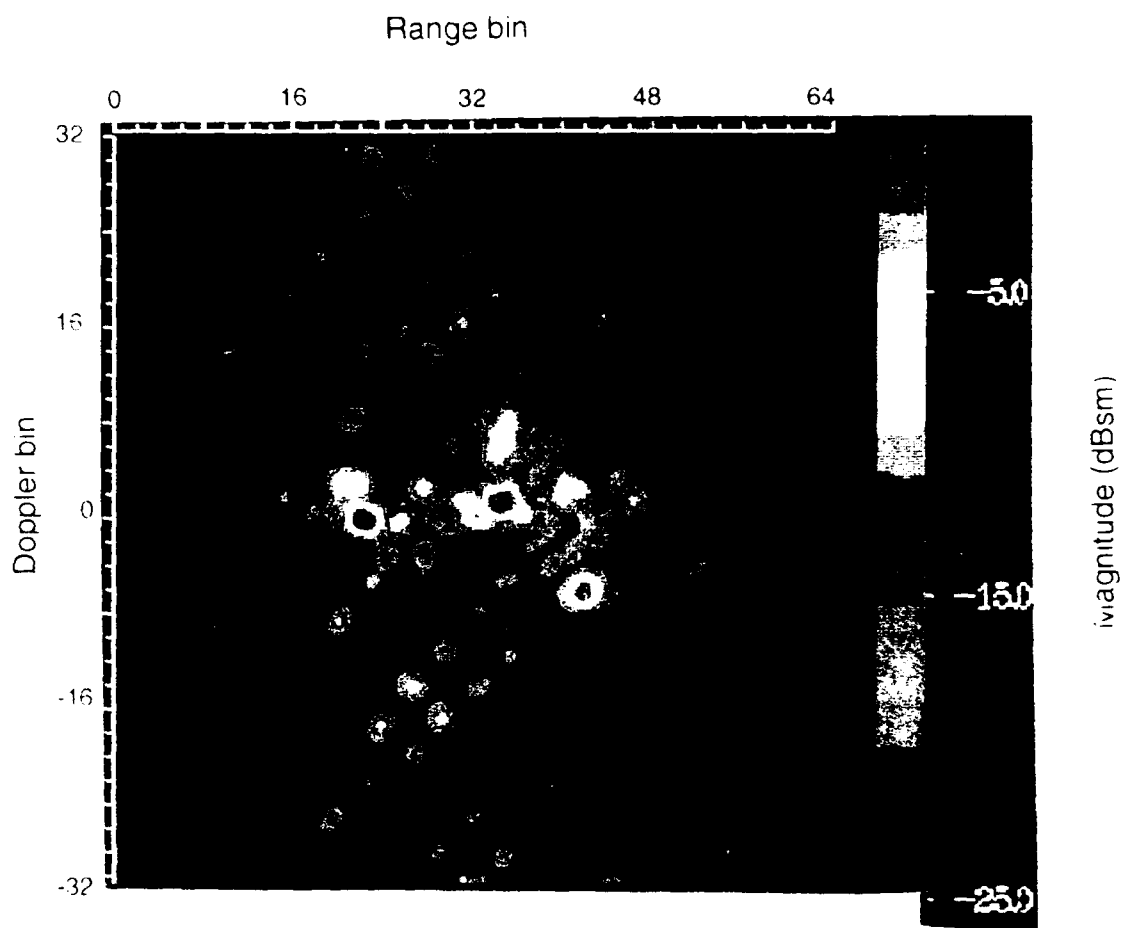


Figure 17. X-band ISAR image taken during circular-orbit flight.

- The relative range and Doppler scale factors are determined by equations (5) and (6), and only a fortuitous circumstance (or careful control of a cooperating target) produces a range-Doppler image that has an aspect ratio that resembles the aspect ratio of a photographic image of the target. By combining equations (5), (6), and (8), if the target angular rate-of-change happens to have a value of

$$\Omega_0 = \frac{B\lambda f_p}{c N_b N_f} \quad (10)$$

then the range and cross-range pixel are clearly equal, and the image will resemble a photograph. Note that this condition is proportional to wavelength. Table 5 gives the value of Ω_0 for the X-band and 49-GHz conditions.

- The apparent target-aspect angle in the ISAR image is not necessarily the same as the actual aspect angle as viewed from the radar; in fact, they are usually much different. The image plane is determined by the rotation axis of the target during the image frame time.

Figures 16 and 17 demonstrate the effect of wavelength in equation (10). The 49-GHz image (figure 16) clearly displays the wings, fuselage, and tail region of the Piper Navajo in an approximate photographic aspect, although the image appears somewhat stretched in the Doppler dimension. This can be expected, because the turn rate of the target can be calculated as $\Omega = 2\pi/147 = 43$ mrad/sec, where 147 seconds is the length of time required for the target to complete the orbit. From table 5, $\Omega_0 = 25$ mrad/sec at 49 GHz, for an expansion in Doppler dimension of about 1.7, as observed.

However, the Doppler axis of the X-band image in figure 17 is compressed (compared to the 49-GHz image) by a factor of five. For example, the ends of the wings, which are prominent because of instrumentation pods at the wingtips, occur approximately at Doppler bin 24 in the X-band image, and at Doppler bin 112 in the 49-GHz image, which is approximately a ratio of 5. Since $\Omega_0 = 134$ mrad/sec at X-band (table 5), a compression in the Doppler dimension by a factor of $42.7/134 = 0.32$ is expected compared to the true target-aspect ratio. In fact, the image does appear to be compressed by approximately this amount in the Doppler dimension.

The most significant observation is the plethora of fine features that show up in the 49-GHz image. In particular, numerous scattering centers are evident along the wings, presumably arising from the wing-panel joints, slots, rivets, and other structures that scatter significantly at 49 GHz. Brightest in the image are scattering centers associated with the junction of the wings and tail with the fuselage.

The engine nacelles and associated air intakes, which produce significant scattering on many airborne targets, are not observed in these images, nor are they a major scatterer in other images. The relatively streamlined nacelles (figure 8) apparently do not produce significant backscatter, except at the head-on incidence angle of figure 13.

The X-band image is dominated by four large scattering centers, without much fill-in detail. We emphasize that this X-band image is typical of other X-band images computed from this portion of the flight; that is, this image is not abnormal. The major reason for less detail in the Doppler dimension is the larger cross-range pixel size at X-band (93 cm, compared with 17 cm at 49 GHz; see table 5). However, to obtain a cross-range pixel size of 17 cm at X-band would require a frame number five times the $N_f = 64$ used here. Increasing the frame number presents two problems.

- The aperture time is five times as long. Instead of the 0.4 sec required for each frame at $N_f = 64$, a time of 2.0 sec would be required. The longer time would affect scan rates and dwell times in an operational radar.
- The motion compensation is more difficult as T_f increases, since the target motion is more likely to have a nonuniform rotation rate. This situation requires estimates of rotation acceleration, and possibly higher order terms, to give acceptable images.

The 49-GHz radar clearly produces a superior image in a significantly reduced observation time.

Also evident in the X-band image are aliased responses from propeller returns produced by a sampling rate (i.e., the burst frequency) that undersamples the rotating propeller. The propeller aliasing is not evident at 49 GHz in this particular image—for reasons not clearly understood. However, propeller aliases can be observed in other 49-GHz images.

Figure 18 is another example of a 49-GHz image taken during a circular-orbit flight. This image is particularly outstanding in showing a significant amount of detail; it also (fortuitously) has an aspect ratio close to that of a photographic image of the target.

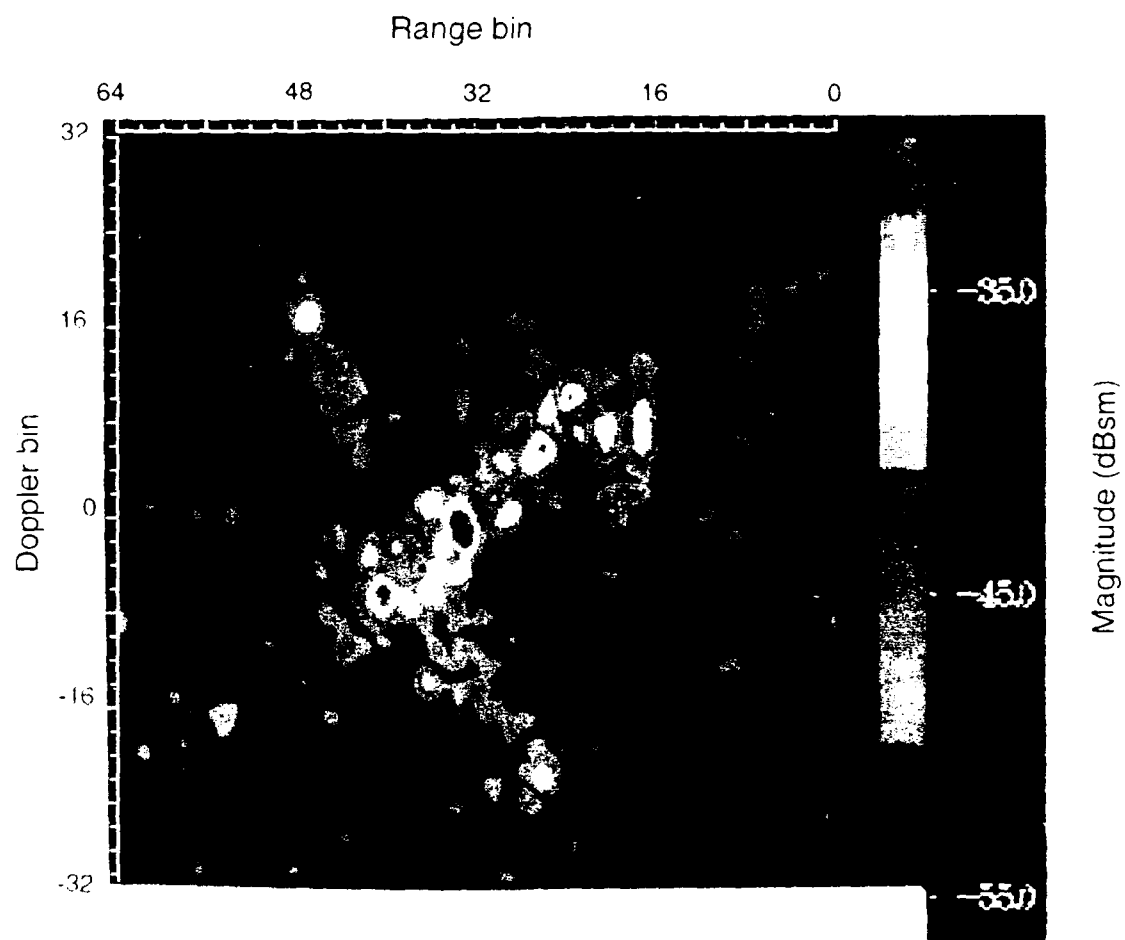


Figure 18 49-GHz ISAR image taken during circular-orbit flight.

9.0 SUMMARY AND CONCLUSIONS

We have conducted simultaneous measurements of the RCS of an airborne Piper Navajo twin-engine aircraft at 9.0 and 49.0 GHz. The RCS at 49 GHz was always found to be higher than at 9 GHz by an amount that depended on the target-aspect angle. The largest increase was 19 dB and was measured at nose-on incidence; at other angles of incidence, the increase ranged from 3 to 10 dB. The increase averaged over a 360-degree aspect-angle change was 8 dB.

High-quality inverse synthetic aperture radar (ISAR) images were obtained at 49 GHz with an aperture time of only 0.41 sec. The same resolution in cross-range at 9 GHz would have required an aperture time of least 2.2 sec. The 49-GHz ISAR images showed scattering from small details that tended to fill in the target shape and produce an outline view of the target. This outlining of the target, which is typically not the case for X-band images (they are typically dominated by a few strong scatterers), should make noncooperative target identification (NCTI) more straightforward for millimeter-wavelength radars.

10.0 REFERENCES

1. Radar Branch. 1990. "Radar Cross Section Data Collection and Processing Capabilities." NOSC TD 1802 (April). Naval Ocean Systems Center, San Diego, CA. UNCLASSIFIED.
2. Ruck, G. T., D. E. Barrick, W. D. Stuart, and C. K. Krichbaum. 1970. *Radar Cross Section Handbook*, pp. 141-202. Plenum Press, New York. UNCLASSIFIED.
3. Currie, N. C., and C. E. Brown (Ed.). 1987. *Principles and Applications of Millimeter-Wave Radar*. Artech House, Boston. UNCLASSIFIED.
4. Bhattacharyya, A. K. and D. L. Sengupta. 1991. *Radar Cross Section Analysis and Control*. pp. 172-173. Artech House, Boston. UNCLASSIFIED.
5. Wehner, D. R. 1987. *High Resolution Radar*. Artech House, Boston. UNCLASSIFIED.
6. Bocker, R. P., T. B. Henderson, S. A. Jones, and B. R. Frieden, "A New Inverse Synthetic Aperture Radar Algorithm for Translational Motion Compensation," to be published in *Journal of Image Processing*. UNCLASSIFIED.

REPORT DOCUMENTATION PAGE

Form Approved
OMB No. 0704-0188

Public reporting burden for this collection of information is estimated to average 1 hour per response, including the time for reviewing instructions, searching existing data sources, gathering and maintaining the data needed, and completing and reviewing the collection of information. Send comments regarding this burden estimate or any other aspect of this collection of information, including suggestions for reducing this burden, to Washington Headquarters Services, Directorate for Information Operations and Reports, 1215 Jefferson Davis Highway, Suite 1204, Arlington, VA 22202-4302, and to the Office of Management and Budget, Paperwork Reduction Project (0704-0188), Washington, DC 20503

1. AGENCY USE ONLY (Leave blank)		2. REPORT DATE January 1993		3. REPORT TYPE AND DATES COVERED Final FY 91 - FY 93	
4. TITLE AND SUBTITLE MEASUREMENTS OF THE RADAR CROSS SECTION AND INVERSE SYNTHETIC APERTURE RADAR (ISAR) IMAGES OF A PIPER NAVAJO AT 9.5 GHz AND 49 GHz				5. FUNDING NUMBERS PR: SXB2 PE: 0603013N TA: 75-SX10 Access No: DN309101	
6. AUTHOR(S) R. Dinger, G. Kinzel, W. Lam, S. Jones					
7. PERFORMING ORGANIZATION NAME(S) AND ADDRESS(ES) Naval Command, Control and Ocean Surveillance Center (NCCOSC) RDT&E Division San Diego, CA 92152-5001				8. PERFORMING ORGANIZATION REPORT NUMBER NRaD TR 1569	
9. SPONSORING/MONITORING AGENCY NAME(S) AND ADDRESS(ES) Space and Naval Warfare Systems Command Washington, DC 20363				10. SPONSORING/MONITORING AGENCY REPORT NUMBER	
11. SUPPLEMENTARY NOTES					
12a. DISTRIBUTION/AVAILABILITY STATEMENT Approved for public release; distribution is unlimited.				12b. DISTRIBUTION CODE	
13. ABSTRACT (Maximum 200 words) Studies were conducted of the enhanced radar cross section (RCS) and improved inverse synthetic aperture radar (ISAR) image quality that may result at millimeter-wave (mmw) frequencies. To study the potential for mmw radar in these areas, a program was initiated in FY 90 to design and fabricate a 49.0- to 49.5-GHz stepped-frequency radar. After conducting simultaneous measurements of the RCS of an airborne Piper Navajo twin-engine aircraft at 9.0 and 49.0 GHz, the RCS at 49.0 GHz was always found to be higher than at 9.0 GHz by an amount that depended on the target-aspect angle. The largest increase was 19 dB and was measured at nose-on incidence; at other angles of incidence, the increase ranged from 3 to 10 dB. The increase averaged over a 360-degree aspect-angle change was 7.2 dB. The 49.0-GHz radar has demonstrated a capability to gather well-calibrated millimeter-wave RCS data of flying targets. In addition, the successful ISAR images obtainable with short aperture time suggest that 49.0-GHz radar may have a role to play in noncooperative target identification (NCTI).					
14. SUBJECT TERMS millimeter-wave (mmw) radar frequencies radar cross section (RCS) data inverse synthetic aperture radar (ISAR) images				15. NUMBER OF PAGES 49	
17. SECURITY CLASSIFICATION OF REPORT UNCLASSIFIED				16. PRICE CODE	
18. SECURITY CLASSIFICATION OF THIS PAGE UNCLASSIFIED		19. SECURITY CLASSIFICATION OF ABSTRACT UNCLASSIFIED		20. LIMITATION OF ABSTRACT SAME AS REPORT	

UNCLASSIFIED

21a. NAME OF RESPONSIBLE INDIVIDUAL R. Dinger	21b. TELEPHONE (Include Area Code) (619) 553-2500	21c. OFFICE SYMBOL Code 755

INITIAL DISTRIBUTION

Code 0012	Patent Counsel	(1)
Code 70	R. E. Shutters	(1)
Code 75	J. E. Griffin	(1)
Code 755	R. J. Dinger	(20)
Code 961	Archive/Stock	(6)
Code 964B	Library	(2)

Defense Technical Information Center Alexandria, VA 22304-6145	(4)	Naval Air Warfare Center Aircraft Division Warminster, PA 18974-5000	(3)
NCCOSC Washington Liaison Office Washington, DC 20363-5100		Advanced Research Projects Agency Arlington, VA 22203-1714	
Center for Naval Analyses Alexandria, VA 22302-0268		Wright-Patterson AFB Ohio 45433-9543	(3)
Navy Acquisition, Research and Development Information Center (NARDIC) Washington, DC 20360-5000		6585TH Test Group/PR Holloman AFB, NM 88310-5000	
GIDEP Operations Center Corona, CA 91718-8000		Georgia Institute of Technology Atlanta, GA 30332	(2)
NCCOSC Division Detachment Warminster, PA 18974-5000		Dynamics Technology, Inc. Torrance, CA 90503-2117	(2)
Chief of Naval Operations Washington, DC 20350		Flam & Russell, Inc. Horsham, PA 19044	
Naval Research Laboratory Washington, DC 20375-5000	(14)	Global Associates, LTD Arlington, VA 22201	
Naval Sea Systems Command Washington, DC 20362-5101	(2)	Hughes Aircraft Company Los Angeles, CA 90009	(5)
Office of Naval Research Arlington, VA 22217-5000	(3)	Lockheed Missiles/Space Company Palo Alto, CA 94304-1191	
Naval Surface Warfare Center Dahlgren Division Detachment Silver Spring, MD 20903-5000		MIT Lincoln Laboratory Lexington, MA 02173-0073	(2)
Naval Surface Warfare Center Carderock Division Bethesda, MD 20084-5000		Symmetron, Inc. Fairfax, VA 22030-5009	
Naval Air Warfare Center Weapons Division China Lake, CA 93555-6001	(6)	Telephonics Farmingdale, NY 11735 United Technologies Norwalk, CT 06856-5300 Westinghouse Electric Corporation Baltimore, MD 21203	(2)